

## ARTICLE OPEN

Coating two-dimensional MoS<sub>2</sub> with polymer creates a corrosive non-uniform interfaceQuoc Huy Thi<sup>1</sup>, Hyun Kim<sup>2,3</sup>, Jiong Zhao<sup>4,5</sup> and Thuc Hue Ly<sup>1</sup>

Two-dimensional (2D) materials and soft materials are both susceptible to mechanical instabilities, such as buckling, wrinkling, folding and creasing, especially when located on surfaces. Here, we report that weak van der Waals interactions cause the interface between 2D molybdenum disulphide (MoS<sub>2</sub>) and a soft poly(methyl methacrylate) coating to demonstrate mechanical instability and delamination. The resulting non-uniform and buckled interface greatly hampers the ability of the coating to protect the MoS<sub>2</sub> substrate. Also, the corrosion rate of 2D MoS<sub>2</sub> and quench rate of intrinsic luminescence in 2D MoS<sub>2</sub> were significantly accelerated by the soft coating. Owing to the formation of corrosive cavities at the interface, the geometry and size of the flakes became the dominating factor, and a critical size of 2D flakes for such interfacial instability was determined based on elasticity theory. Such hazardous corrosion in a 2D material caused by a soft coating raises concern for their use in electronic packaging, and for the processing of van der Waals-layered materials for future applications.

npj 2D Materials and Applications (2018)2:34; doi:10.1038/s41699-018-0079-x

## INTRODUCTION

Empowered by their atomic thickness, the emergent two-dimensional (2D) materials<sup>1,2</sup> nowadays attract a lot of attention. However, similar to many other low-dimensional materials, they have the notable drawback of poor stability and robustness, which is mainly owing to their large surface ratio and surface/edge activities. In particular, as one group of promising 2D materials, transition metal dichalcogenides (TMDs) can be applied for electronic and optoelectronic devices, such as light emitting diodes, photodetectors, solar cells or lasers.<sup>3–5</sup> However, the 2D TMDs have been found unstable under ambient conditions,<sup>6,7</sup> which narrows their applications. Though it is also noted the active edge sites of TMD monolayers may be passivated by the TiN substrates,<sup>8</sup> and monolayers are more resistant to electroablation compared with the bulk.<sup>9</sup> To tackle inherent degradation problems including oxidation, hydration or impurity adsorptions in 2D materials, special precautions need to be taken in their fabrication, processing and packaging.

The main concept for protection is blocking the chemically aggressive environments by the coating layer or inert passivation.<sup>10</sup> In the electronics industry today, active materials are conventionally packaged/protected by metal, ceramic or polymer shells/coatings,<sup>11</sup> particularly for microelectronic devices with high requirements on stability, power density, conductivity, compatibility and integrity. Analogously, for the 2D materials, the protective packaging become indispensable in various applications, especially under some harsh working conditions. Soft coating using polymers such as Poly (methyl methacrylate) (PMMA), polydimethylsiloxane or epoxy<sup>12</sup> is economic and facile for processing, however, as we will discuss in current work, the role played by interfaces along with 2D materials is decisive for

the performances of these coating. In fact the 2D material/soft matter interfaces have been widely applied in transferring/printing/processing for various applications,<sup>13,14</sup> and these interfaces concerned are essential for the structural/morphological control and physical property tailoring, as well as for the performances of flexible devices using soft substrates.

Despite 2D materials being highly flexible<sup>15–17</sup> and easily coupled with various surfaces, it is well known the 2D materials have weak interlayer interactions, mostly via the van der Waals (vdW) interactions with the external environments. Therefore, instability and delamination at the interfaces between 2D materials and attached surfaces regularly occurs.<sup>18,19</sup> Alternatively, artificial out-of-plane covalent bonding may enhance the adhesion between the 2D layers and external surfaces, nevertheless the ground breaking properties in 2D materials may be lost.<sup>20</sup> Thus, the packaging/coating of 2D materials faces the trade-off problem for coating, and the interfacial instability/delamination control is the key of protective layers.

In this work, we will demonstrate that coating by soft materials such as PMMA on 2D MoS<sub>2</sub> inevitably releases the internal stresses or interfacial stresses by mechanical instability. The resulting non-uniform interfaces and aggressive environments built up in the micro-cavities at interfaces can rapidly trigger remarkable corrosion in the 2D materials, which is opposed to our primary purposes of protective coatings. Such corrosion under protection is nucleated homogeneously inside the flakes, distinct to the samples without protection where the corrosion is initialised from the edges. The geometry and size of flakes dominate the corrosion rate, which can be rationalised by the elastic buckling theory. This unexpected enhanced corrosion behaviour resembles the famous corrosion under insulation (CUI) events, as recognised by the

<sup>1</sup>Department of Chemistry and Center of Super-Diamond & Advanced Films (COSDAF), City University of Hong Kong, Hong Kong, China; <sup>2</sup>Center for Integrated Nanostructure Physics (CINAP), Institute for Basic Science (IBS), Suwon 16419, Korea; <sup>3</sup>Department of Energy Science, Department of Physics, Sungkyunkwan University (SKKU), Suwon 16419, Korea; <sup>4</sup>The Hong Kong Polytechnic University Shenzhen Research Institute, Shenzhen, China and <sup>5</sup>Department of Applied Physics, The Hong Kong Polytechnic University, Kowloon, Hong Kong, China

Correspondence: Thuc Hue Ly (thuchly@cityu.edu.hk)

Received: 16 April 2018 Revised: 14 August 2018 Accepted: 20 August 2018

Published online: 19 October 2018

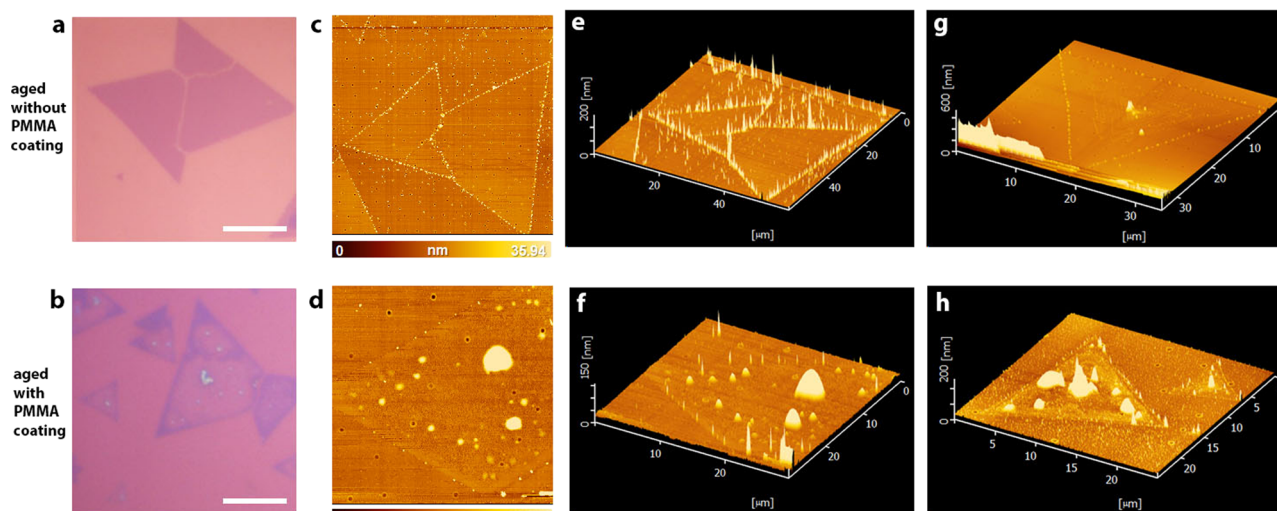


**Fig. 1** The comparison of aging effects on bare **a, c, e, g** and PMMA-coated **b, d, f, h** 2D MoS<sub>2</sub> for 1 month in ambient conditions. **a** Optical micrographs for the aged monolayer(1 L)-MoS<sub>2</sub> without coating. Scale bar is 5 μm. **b** Optical micrographs for the aged 1L-MoS<sub>2</sub> with PMMA coating. Scale bar is 5 μm. **c, d** AFM topographic images for the without coating and PMMA-coated 1L-MoS<sub>2</sub> after aging. **e, f** The 3D layouts corresponding to **c, d**, respectively. **g, h** The 3D AFM topographic layouts of another pair of without coating and with PMMA coating 2D spiral MoS<sub>2</sub> samples after aging

industry from 1970s.<sup>21</sup> Owing to the weak-bonding nature at interfaces involving the 2D materials<sup>22</sup> and various physical/chemical properties governed by the interfaces concerned,<sup>23–25</sup> in-depth understanding of such interfacial instability is important.

## RESULTS AND DISCUSSIONS

PMMA is regarded as one of the most promising soft coating materials owing to its low moisture adsorption rate, good resistance to acids, alkalis and weathering.<sup>26</sup> Most importantly, it is economic and compatible with large-scale fabrications in industry.<sup>27</sup> 2D molybdenum disulphide (MoS<sub>2</sub>) we used for the current study was synthesised by chemical vapour deposition (CVD) (see Methods for details) on SiO<sub>2</sub>/Si wafer. The as-synthesised samples were divided into three parts for further stability tests. The first part is for PMMA protection layer coating. A thin layer of PMMA was spin-coated on the surfaces at a speed of 2000 rpm. The PMMA thickness (data available for the commercial PMMA-A4 solvent, <http://microchem.com/>) is ~300 nm. The PMMA-coated samples was then dried in room temperature for sufficient time. Meanwhile, control groups were prepared using the original 2D MoS<sub>2</sub> (as-synthesised ones on SiO<sub>2</sub>/Si substrates and post-transfer ones on other SiO<sub>2</sub>/Si substrates). Then all the samples were safely stored under ambient conditions (~20 °C, RH ~50%) for one to six months before further characterisation.

Surprisingly, the aging results turned out that all the samples were corroded, whereas the corrosion rate were quite dispersive. For samples without PMMA coating (control group), the optical images (Fig. 1a) revealed that except at the grain boundaries some nano-cracks are formed, no cracking or apparent particles can be found. This is in line with the fact that edges or grain boundaries are the most active positions where the corrosions can be selectively initialised. In contrast, samples with protective PMMA coating showed much stronger corrosion. Figure 1b exhibited the strong corrosion occurred inside the flakes under the PMMA coating, despite the edges were maintained safely.

The surface morphologies of the aged samples were studied using atomic force microscopy (AFM) (Fig. 1c–h). Note the samples with PMMA coating were cleaned by acetone right before the AFM measurements. We examined two types of CVD samples: monolayer and multilayer (spiral) MoS<sub>2</sub>.<sup>28</sup> The edge corrosion was stronger on the bare MoS<sub>2</sub> samples than the PMMA captured

samples (Fig. 1c–f). Supplementary Figure S1 shows the line profile crossing the oxidised edge on a bare spiral sample, a width of ~500 nm and height of ~10 nm was observed, which is thickness independent. Conversely, a much smaller width of ~200 nm and height of ~20 nm was recorded for the sample coated with PMMA (Supplementary Figure S1). It is noteworthy that the centre of MoS<sub>2</sub> flake started to be corroded under the PMMA protective layer, and bulky particles (~1–2 μm in width and 100 nm in height, attributed to the formation of MoO<sub>x</sub>) were formed in PMMA-protected samples (Fig. 1d, f, h), in comparison, no particles appeared yet on the bare MoS<sub>2</sub>.

The scanning electron microscopy (SEM) clearly revealed the different corrosion behaviour after long time aging (~6 months) for bare and PMMA-coated 2D flakes, respectively (Fig. 2a, b). For 2D TMDs, the optical signals are good figure-of-merit for the material/structural quality.<sup>29</sup> Our samples were investigated by confocal photoluminescence (PL) and Raman spectroscopy at room temperature. Figure 2c, d shows the PL intensity-integrated mapping by applying an area filter with integrated the A peak (640–700 nm) and Supplementary Figure S2 presents the B peak (700–740 nm) position mapping on the multilayer spiral samples. The dropped down intensity at the edges implied the edge oxidation on bare MoS<sub>2</sub> samples. The PL intensity undergoes a sudden surge followed by gradual decrease from the edge to the centre, correlated with the decrease of thickness in the spiral sample (Fig. 2c). Owing to the direct bandgap nature of monolayer MoS<sub>2</sub>, PL intensity is strongest in 1 L and decreases with increasing layer thickness owing to the direct-to-indirect bandgap transition.<sup>30</sup> On the other hand, PL integrated (A peak) mapping on the PMMA-protected samples filter showed the extreme degradation in the thinner part, indicating strong corrosion (Fig. 2d). Similar trend was observed for the B peak filter mapping as well.

The results from Raman integrated map (Fig. 2e, f) are in line with the PL mapping. The Raman spectrum (Supplementary Figure S3) exhibits the presence of the characteristic E<sub>2g</sub> (381 cm<sup>-1</sup>) and A<sub>1g</sub> (400.5 cm<sup>-1</sup>) modes. The obtained A<sub>1g</sub>/E<sub>2g</sub> ratio was larger than 1, indicating the oxidation is present on the whole PMMA-protected sample. Raman signal was much weaker in the PMMA-coated sample compared with bare samples, mainly owing to corrosion in the entire monolayer part (Fig. 2f). In addition, the comprehensive X-ray photoelectron spectroscopy (XPS) results exhibited more oxidation evidences (e.g., Mo 3d p<sub>3/2</sub> and p<sub>5/2</sub>

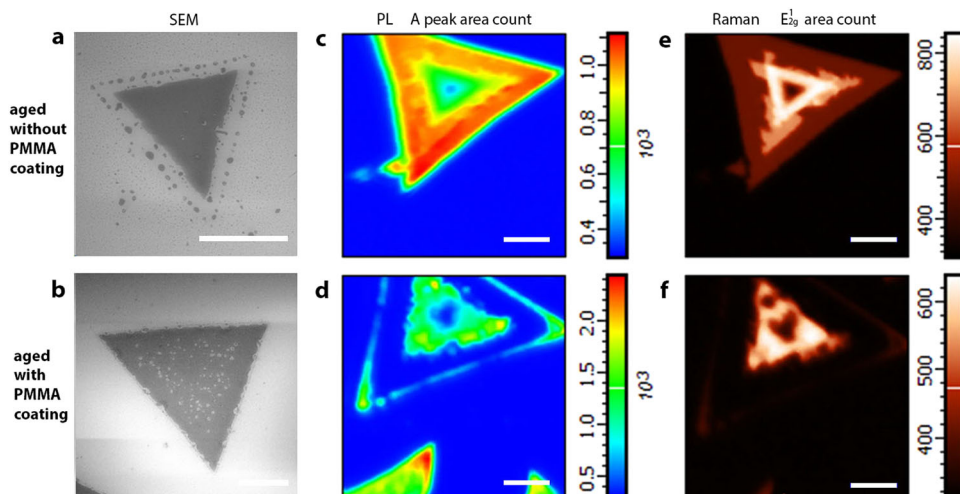


**Fig. 2** SEM, PL and Raman characterisations on 6 month aged samples. **a, b** SEM micrographs of the 1L-MoS<sub>2</sub> without coating and with PMMA coating after aging. Scale bars are 20  $\mu\text{m}$ . **c, d** PL spectrum mapping using A exciton peak area of 2D spiral type MoS<sub>2</sub>, without and with PMMA coatings after aging, respectively. Scale bars, 5  $\mu\text{m}$ . **e, f** Raman spectrum mapping using E<sub>12g</sub> peak area of 2D spiral type MoS<sub>2</sub>, without and with PMMA coatings after aging, respectively. Scale bars, 5  $\mu\text{m}$

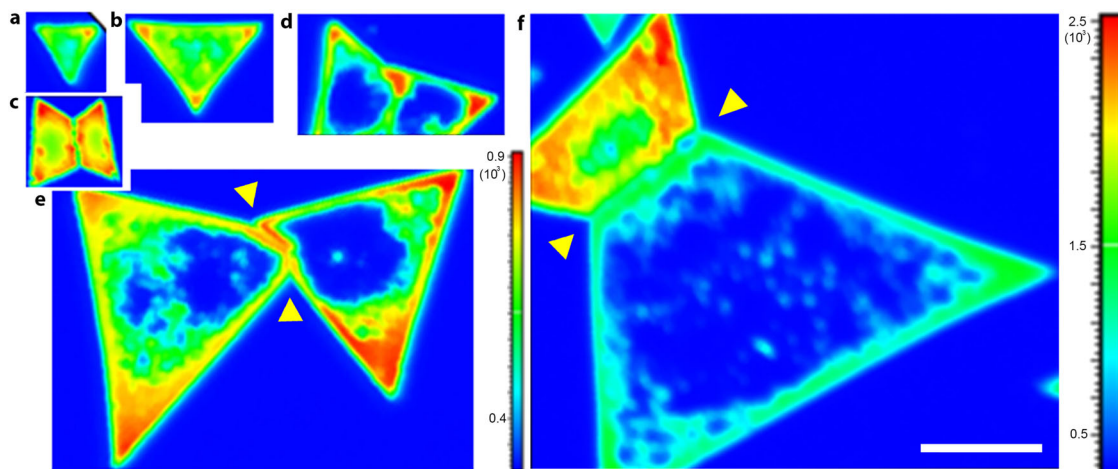


**Fig. 3** The PL spectrum mapping using A exciton peak on different size and geometry 1L-MoS<sub>2</sub> flakes (all with PMMA coating) after 1 month aging. **a–f** All the flakes are rescaled in the same magnification. The yellow arrows mark the domain boundaries. The unified lateral scale bar in **f** is 10  $\mu\text{m}$ . The colour bar (PL intensity, unit: counts) for **a–e** is shown in **e**, and colour bar for **f** is shown in panel **f**

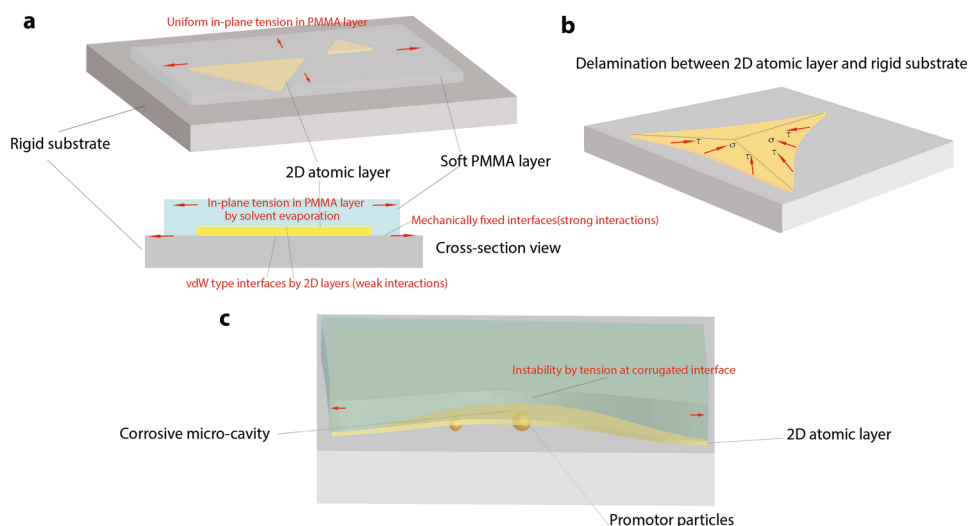
peaks) in the aged samples (see supplementary Figure S4), whereas the PMMA-coated samples still have much higher oxidation signatures than the bare samples. The Transmission electron microscopy (TEM) result and electron energy loss spectroscopy (EELS) data acquired from the aged samples (see supplementary Figure S5 and S6) also clearly exhibit the trace of oxygen. It is clearly seen in the above results that the dynamics of corrosion here include two parts, nucleation and growth. The nucleation sites ( $\sim 1$  month) for 2D layers with and without coatings are distinct (Fig. 1), further, the growth of the corrosion pits (1 month to 6 months) occurs following the nucleation, at the edges or inside flakes, respectively.

For monolayer MoS<sub>2</sub>, the PL intensity are quenched to  $< 1\%$  after corrosion, over two order of magnitude difference in intensity, see supplementary Figure S7. Thus, regarding to the portion of oxidised area in the monolayer MoS<sub>2</sub>, the intensity in the PL images can be linearly mapped to the percentage of corrosion area already taken place in the monolayer MoS<sub>2</sub>.

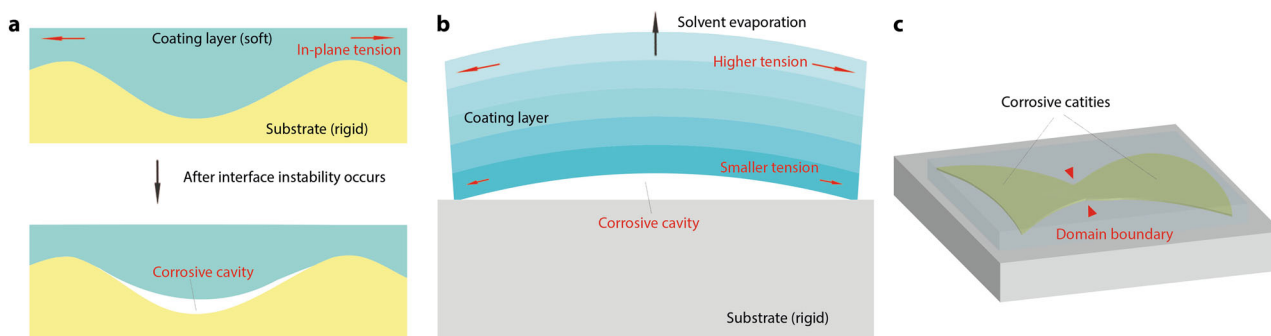
More interestingly, a strong size and geometry dependence of the corrosion rate were found in the PMMA-protected 2D flakes.

Figure 3 shows the distinct corrosion results by PL mapping of PMMA-protected samples after 1 month aging. All the images are presented in the same scale (with unified lateral scale bar in Fig. 3f). It is evident under similar conditions smaller flakes are much less damaged than bigger flakes. The corruptions in 1L MoS<sub>2</sub>, which includes domain boundaries (in bowtie shape) show more features (Fig. 3c–f). In the PL intensity map (A peak) without PMMA protective layer, except for the corrosion-preferred domain boundaries, the corrosion rate is quite uniform for different domain sizes. However, in the presence of the PMMA protective layer, the larger domain has much faster corrosion (Fig. 3f), and the corrosion rate was close when the domain sizes are in equal (Fig. 3d, e).

The above observations suggested correspondences between the corrosion enhancement effect and the soft layer (PMMA) coating. The CUI occurred mainly as the protective (insulation) layer captures the water, oxygen or other reactive species underneath, which build up highly corrosive and closed micro-environment for the surface of metals.<sup>31</sup> Thereby, in our experiments the PMMA coating has played similar roles. Sketched



**Fig. 4** The schemes for the corrosive interfaces. **a** 3D(upper) and cross-section views(lower) of the experimental specimens coated with PMMA. **b** The delamination between 2D layer and substrate caused by cooling after synthesis. **c** The delamination between 2D layer/substrate and 2D layer/soft coating



**Fig. 5** The instability mechanisms at the interfaces. **a** The buckling and cavity formation by corrugations at interfaces. **b** The instability caused by stress gradient originated from inhomogeneous evaporation of solvents. **c** The scheme for bowtie shape 2D flakes with buckling inside domains rather than at domain boundaries (red arrows). 2D atomic layers at the interface are not shown, they might be attached either to the soft coating or the rigid substrate after buckling

in Fig. 4a, there are mainly three parts involved, the stiff substrate (Si/SiO<sub>2</sub> wafer), the 2D atomic layer (MoS<sub>2</sub>) and the soft coating (PMMA). Our previous work has revealed the interfacial mismatch between the stiff substrates and 2D layers.<sup>18</sup> The homogeneous in-plane tensile stress may induce edge instability and delamination once the interfacial stress is over the critical value (Fig. 4b). The delaminated 2D parts and interfacial cavity will grow under the combination of tension and shear stress.

As the commanding requirement of interfacial delamination, interactions between the 2D layers and the substrate or 2D layers and the PMMA coatings are vdW type, which are weak bonding compared with the stronger interactions between the PMMA and Si/SiO<sub>2</sub> substrates. This is based on the fact that carboxyl (of PMMA)-oxygen (of Si wafer) bonding is stronger than the vdW bonding along MoS<sub>2</sub>, hence we can neglect the interactions involving 2D MoS<sub>2</sub>. The second condition for instability is stress condition. The overall residual stress remained in the PMMA layer after evaporation of solvent is tensile (in-plane).<sup>32</sup> Fig. 4a, c has depicted the residual stresses in the 2D layers and soft coatings. In our samples, the 2D atomic layers are not continuous full films. As we mentioned the instability at PMMA/2D layer and 2D layer/substrate interfaces will be favoured owing to weak bonding, and the interfaces between PMMA/substrate can be reckoned as rigid (fixed), hence uniform in-plane tensile stress in the entire PMMA coatings cannot induce any instability. Nevertheless, the CVD

growth of 2D layers inevitably introduces some promoter particles or reactant material particles on/underneath the 2D layers (see Methods section), which can trigger out-of-plane fluctuations or corrugations in 2D layers. The wrinkles in the 2D layers can also cause corrugations. Therefore, the soft coatings (PMMA) will have corrugated inner surfaces (PMMA/2D layer interfaces) accordingly. Moreover, for 2D multilayer samples, such as the spirals in Fig. 1, the inner surfaces of PMMA (PMMA/2D layer interface) are naturally corrugated. Thus, under tensile stress the corrugated soft surfaces where Gaussian curvature larger than zero will cause instability buckling and delaminations (see Fig. 5a).

The PMMA/substrate interfaces are firmly fixed, whereas the PMMA/2D layer or 2D layer/substrate interfaces experience instabilities and micrometre sized cavities at the interfaces are created. Followed by the intake of moisture and oxygen, these cavities act as the ideal corrosive and pressurised micro-chambers. The reaction products (e.g., oxide particles, Fig. 2d) can enlarge or connect the cavities, thus the corrosion become self-catalytic. Eventually, the 2D layers will be selectively corroded from the centre of flakes, whereas the edges of 2D flakes are relatively protected by the PMMA coating, because they are close/attached to the fixed PMMA/substrate interface.

Another source of instability comes from inhomogeneous stress/modulus gradient along thickness direction of the soft coating layers. For the solvent evaporation is outward (Fig. 5b) and

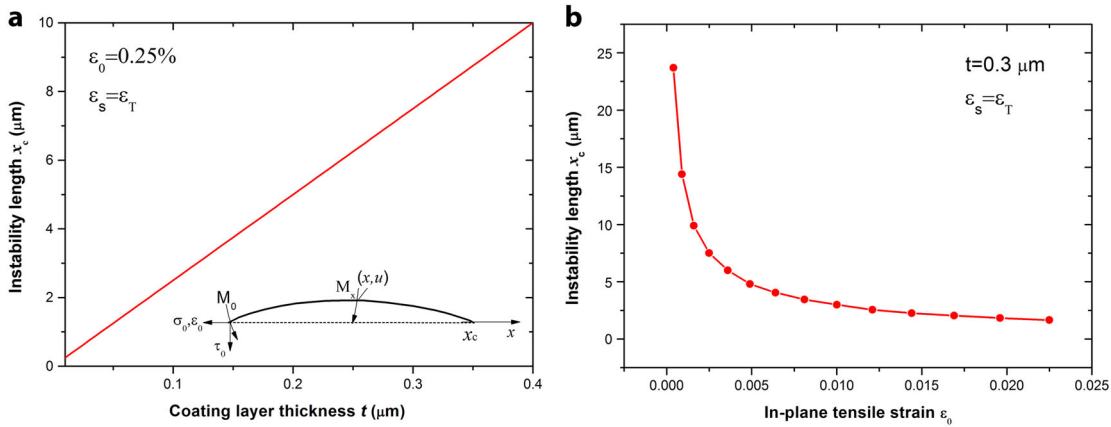


**Fig. 6** Modelling results by the elastic theory. **a** The instability length-coating thickness plot. Lower-right corner inset shows the model and definitions. **b** The instability length-tensile strain(residual) plot. Respective conditions are indicated at corners

opposite to the PMMA/2D layer or 2D layer/substrate interfaces, the evaporation will be more complete close to outward surfaces than the inward interfaces, thus higher tension will remain close to the outward surfaces. This stress gradient can introduce bending moment and finally cause the interfacial instability once reaching the critical point/condition. The consequent corrosive chambers for the 2D flakes by the stress gradient and the local corrugations as discussed in previous paragraphs play as the main sources of CUI.

Following the above analysis, the size and geometry dependence of the corrosions in 2D flakes can be readily understood. Assume the density of corrugations at the interfaces are uniform, firstly the larger flakes will have higher possibility to have corrugation-induced instability at interfaces; second, the larger flakes will have more instability induced cavities, and form larger corrosive chambers after the cavities/buckling are spatially connected or buckled by stress gradient along thickness direction of coatings, which can accommodate larger volume and higher diffusivity for the reactants. Compared with the high-symmetrical (threefold) triangle shaped flakes, the anisotropic bowtie shape flakes, which consist of two single domains have two main axis, which will cause distinct amplitudes in the buckling (Fig. 5c). No buckling or minute buckling occurs at the domain boundaries (arrows in Fig. 5c). Thereby the corrosion rate is much larger inside the domains than at the domain boundaries.

We can further apply the elastic theory for buckling<sup>33</sup> on the above systems. Consider the 1D instability case in small deformation approximation with fixed support ends, see Fig. 6a inset. Although whether the 2D atomic layer is attached to PMMA layer or rigid substrate after buckling is uncertain, because the 2D layer is ultrathin as compared with the PMMA layer, only PMMA layer will be considered in our analysis. The governing equation on the post-buckling coating layer is

$$EI \frac{d^2 u}{dx^2} - A\sigma_0 u + A\tau_0 x + M_0 = 0, \quad (1)$$

where  $u$  is deflection of the coating layer,  $I$  is the moment of inertia,  $E$  is isotropic elastic modulus,  $A$  is cross-section area,  $\sigma_0$ , and  $\tau_0$  and  $M_0$  is the normal stress, shear stress (both in  $x$  direction) and bending moment at the original point, respectively. Note, only the interfaces involving 2D vdW layers can be delaminated easily, the soft coating/rigid substrate interfaces are considered as fixed boundary condition in modelling. Using the boundary condition  $u(0) = 0$ , the solution of the governing equation is

$$u_x = -\frac{M_0}{A\sigma_0} \exp\left(\sqrt{\frac{A\sigma_0}{EI}}x\right) + \frac{\tau_0}{\sigma_0}x + \frac{M_0}{A\sigma_0}, \quad (2)$$

as on the other fixed end,  $u(x_c) = 0$ ,

$$\exp(kx_c) = \frac{A\tau_0}{M_0}x_c + 1, \quad (3)$$

where  $k = \sqrt{\frac{A\sigma_0}{EI}}$ . Use the rectangular cross-section, moment of inertia  $I = bt^3/12$ , area  $A = bt$  and  $\sigma_0 = E\varepsilon_0$ , as  $t$  is the thickness of the soft coating film,  $\varepsilon_0$  is the in-plane tensile strain and we assume the stress gradient (caused by evaporation, see Fig. 5b) in thickness direction on isotropic materials,  $E_S$  (for PMMA, typically 1.7 GPa) and  $E_T$  (for PMMA, typically 3.2 GPa) are shear and tensile moduli,  $\varepsilon_s$  is shear strain and  $\varepsilon_T$  the surface tensile strain at origin, eventually we got  $\exp(\sqrt{12}\varepsilon_0 \frac{x_c}{t}) = 6 \frac{E_S \varepsilon_s}{E_T \varepsilon_T} \frac{x_c}{t} + 1$ . Thus, it is clearly seen the linear dependence between the critical buckling length ( $x_c$ ) and the thickness ( $t$ ) of the soft coating layer. Figure 6a plots the  $x_c$ - $t$  curve using typical in-plane strain values.

By applying typical strain conditions, we can also numerically plot the relationship between the instability wavelength  $x_c$  and the in-plane tensile strain  $\varepsilon_0$ , see Fig. 6b. Therefore, the calculated intrinsic buckling of soft coating layer allowed by the weak vdW interface matches with the critical 2D flake sizes synthesised by the CVD method in our experiments (5~20  $\mu\text{m}$ , see Fig. 3). For certain thickness of soft coating, the critical instability length defines the minimum size (dimension) of flake for the interfacial buckling, dependent on the residual in-plane stress. It has successfully explained our observations on the flake size dependence of the CUI rate. Unfortunately, such instability falls into the scale of most nano/micro devices relating to the 2D materials, and the enhanced CUI behaviour under buckled coating layer can significantly hamper the performances of devices.

Owing to the ultralow bending rigidity and weak vdW interactions, 2D materials are known to be flexible and easy to buckle. In this work, we have addressed the importance of the interfacial buckling, which is combined with the 2D layers and polymeric soft coatings. The delamination problems between soft coatings and rigid substrates are prevailing in industry.<sup>34,35</sup> Unfortunately, the incorporation of 2D atomic layered materials may further lead to more severe problems. Here, we studied the role of PMMA coating layer in the protection/corrosion of monolayer 2D TMDs. By using AFM correlated with optical techniques such as PL and Raman, it was surprisingly revealed that the corrosion was much stronger in the presence of PMMA layer, resembling the CUI in industry. In addition, we also elucidated the size and geometry dependences of the corrosion rates and realised the importance of coating thickness and residual stress. Therefore, further applications of the 2D layers are advised to account for these particular corrosive interfaces and greater care should be taken against such CUI in 2D materials.

## METHODS

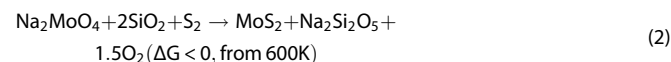
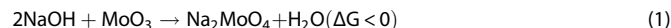
### Preparation of promoter/metal precursor mixture

We purchased iodixanol (Sigma-Aldrich, D1556, solution A), which is used for medium to dissolve promoter and precursor and has no influence on the growth of TMDs. Promoter (solution B) was prepared by dissolving sodium hydroxide (NaOH) in deionized water (0.1 g of NaOH in 80 ml of deionized water). Solution phase ammonium heptamolybdate (AHM) (solution C) and ammonium metatungstate (AMT) (solution D) precursors were also prepared by dissolving ammonium molybdate tetrahydrate (Sigma-aldrich, 431346) in deionized water, respectively.

A total of 11.5 mM AHM was used. Prior to the spin-coating process, solution A, B and C were mixed in an A/B/C ratio of 0.5:3:1. The mixing order (A→B→handshake→C) is critical to prevent micelles generation. The solution was dropped onto the SiO<sub>2</sub>/Si wafer, followed by spin-coating at 3000 rpm for 1 min.

### Growth of MoS<sub>2</sub> monolayer

Two hundred milligrams of S (Sigma-Aldrich, 344621) pellet was loaded into a 2-inch tube furnace in zone 1 and the substrate, which contained the metal precursor was placed in zone 2 (zone for Mo). In this work, the growth was carried out at atmospheric pressure. For the growth, zone 1 was heated up to 210 °C at a rate of 42 °C/min. In the meantime, zone 2 was also heated to 780 °C over a period of 10 min with 2 sccm of H<sub>2</sub> flow. After synthesis process, MoS<sub>2</sub> was formed together with Na<sub>2</sub>Si<sub>2</sub>O<sub>5</sub>, moisture and oxygen. The reaction was described as below:



### Sampling of the aging studies

We have prepared and characterised 14 aged MoS<sub>2</sub> monolayer flakes in-depth with PMMA coating and 13 aged flakes without PMMA coating.

### Characterisation of monolayer TMDs

**PL and Raman spectroscopy.** PL map and Raman spectra were measured by using a multifunctional optical microscopy system (NTEGRA SPECTRA, NT-MDT) with 532 nm laser excitation (~30 μW power) under ambient conditions. The scanned image was obtained at 128 × 128 pixels with a grating of 600 g/mm to yield a spectral resolution of <0.1 cm<sup>-1</sup> for confocal Raman mapping and with a grating of 1800 g/mm to yield a spatial resolution of 200 nm for confocal PL mapping. The accumulation time for each spectrum was 0.3 second for image scanning and 0.5 sec for a single spectrum. An area filter was used to extract the Raman spectrum map with an integration of E<sub>2g</sub> peak (375–392 cm<sup>-1</sup>), A<sub>1g</sub> peak (392–415 cm<sup>-1</sup>) and PL intensity map (640–740 nm).

**AFM characterisation.** The AFM images of samples were recorded using an E-Sweep system (Seiko, Japan) atomic force microscopy. A Au tip (SI-DF3-A) with an ~10 nm tip radius was used. The force constant and resonant frequencies of the tips were approximately 1.9 N/m and 29 kHz, respectively.

**SEM and energy dispersive spectroscopy (EDS).** Field-emission scanning electron microscopy (FESEM) (JSM7000F, Jeol, Japan) was used to examine the surface morphology of samples at different accelerating voltages to obtain a high level of contrast at different magnifications. An X-Max Silicon Drift Detector in a FESEM-JSM7600F system was used for EDS mapping for 10 min. An accelerating voltage of 15 keV was used to obtain sufficiently pronounced signals while retaining sensitivity to the sample surface.

**XPS.** XPS was performed using an Al X-ray source (Thermo-Scientific, ESCALAB 250Xi). All the peaks were measured under high vacuum (10<sup>-8</sup> Torr).

**TEM.** The TEM (STEM) and EELS characterisations were carried out by JEOL ARM 200 F TEM under 80 kV.

## DATA AVAILABILITY

The data sets generated during and/or analysed during the current study are available from the corresponding author on reasonable request.

## ACKNOWLEDGEMENTS

This work was supported by grants from City University of Hong Kong (Project No. 7200551, 9610387), the Hong Kong Polytechnic University Grant (No. 1-ZE8C), Institute for Basic Science (IBS-R011-D1). This work was also supported by the Shenzhen Science and Technology Innovation Commission (Project no. JCYJ20170818104717087).

## AUTHOR CONTRIBUTIONS

T.H.L. directed the work, conducted and analysed the experiment. Q.H.T. conducted the experiment. H.K. provided MoS<sub>2</sub> sample. Z.J. contributed in discussions. T.H.L. and Q.H.T. wrote the manuscript. All authors discussed the results and commented on the manuscript.

## ADDITIONAL INFORMATION

**Supplementary information** accompanies the paper on the *npj 2D Materials and Applications* website (<https://doi.org/10.1038/s41699-018-0079-x>).

**Competing interests:** The authors declare no competing interests.

**Publisher's note:** Springer Nature remains neutral with regard to jurisdictional claims in published maps and institutional affiliations.

## REFERENCES

- Novoselov, K. S. et al. Electric field effect in atomically thin carbon films. *Science* **696**, 666–669 (2004).
- Novoselov, K. S., Mishchenko, A., Carvalho, A. & Neto, A. C. 2D materials and van der Waals heterostructures. *Science* **353**, aac9439 (2016).
- Wang, Q. H., Kalantar-Zadeh, K., Kis, A., Coleman, J. N. & Strano, M. S. Electronics and optoelectronics of two-dimensional transition metal dichalcogenides. *Nat. Nanotech.* **7**, 699–712 (2012).
- Qian, X., Liu, J., Fu, L. & Li, J. Quantum spin Hall effect in two-dimensional transition metal dichalcogenides. *Science* **346**, 1344–1347 (2014).
- Cao, L. Two-dimensional transition-metal dichalcogenide materials: toward an age of atomic-scale photonics. *MRS Bull.* **40**, 592–599 (2015).
- Ye, F. et al. Environmental instability and degradation of single- and few-layer WTe<sub>2</sub> nanosheets in ambient conditions. *Small* **12**, 5802–5808 (2016).
- Venkata Subbaiah, Y. P., Saji, K. J. & Tiwari, A. Atomically thin MoS<sub>2</sub>: a versatile nongraphene 2D material. *Adv. Funct. Mater.* **26**, 2046–2069 (2016).
- Schulman, D. S. et al. Superior electro-oxidation and corrosion resistance of monolayer transition metal disulfides. *ACS Appl. Mater. Inter.* **10**, 4285–4294 (2018).
- Huang, Y. T. et al. Anomalous corrosion of bulk transition metal diselenides leading to stable monolayers. *ACS Appl. Mater. Inter.* **9**, 39059–39068 (2017).
- Mas-Balleste, R., Gomez-Navarro, C., Gomez-Herrero, J. & Zamora, F. 2D materials: to graphene and beyond. *Nanoscale* **3**, 20–30 (2011).
- Seraphim, D. P., Lasky, R. C., & Li, C. Y. Principles of electronic packaging. (McGraw-Hill College, 1989).
- Lau, J. H., Lee, C. K., Premachandran, C. S., & Yu, A. Advanced MEMS packaging. (New York: McGraw-Hill, 2010).
- Kim, S. J., Choi, K., Lee, B., Kim, Y. & Hong, B. H. Materials for flexible, stretchable electronics: graphene and 2D materials. *Annu. Rev. Mater. Res.* **45**, 63–84 (2015).
- Castellanos-Gomez, A. et al. Deterministic transfer of two-dimensional materials by all-dry viscoelastic stamping. *2D Mater.* **1**, 011002 (2014).
- Zhao, J. et al. Two-dimensional membrane as elastic shell with proof on the folds revealed by three-dimensional atomic mapping. *Nat. Commun.* **6**, 8935 (2015).
- Akinwande, D., Petrone, N. & Hone, J. Two-dimensional flexible nanoelectronics. *Nat. Commun.* **5**, 5678 (2014).
- Lee, G. H. et al. Flexible and transparent MoS<sub>2</sub> field-effect transistors on hexagonal boron nitride-graphene heterostructures. *ACS Nano* **7**, 7931–7936 (2013).
- Ly, T. H., Yun, S. J., Thi, Q. H. & Zhao, J. Edge delamination of monolayer transition metal dichalcogenides. *ACS Nano* **11**, 7534–7541 (2017).
- Brennan, C. J., Nguyen, J., Yu, E. T. & Lu, N. Interface adhesion between 2D materials and elastomers measured by buckle delaminations. *Adv. Mater. Inter.* **2**, 1500176 (2015).

20. Xu, Y. et al. A graphene hybrid material covalently functionalized with porphyrin: synthesis and optical limiting property. *Adv. Mater.* **21**, 1275–1279 (2009).
21. De Vogelaere, F. Corrosion under insulation. *Proc. Saf. Prog.* **28**, 30–35 (2009).
22. Geim, A. K. & Grigorieva, I. V. Van der Waals heterostructures. *Nature* **499**, 419–425 (2013).
23. Yu, A., Ramesh, P., Itkis, M. E., Bekyarova, E. & Haddon, R. C. Graphite nanoplatelet – epoxy composite thermal interface materials. *J. Phys. Chem. C* **111**, 7565–7569 (2007).
24. Schmidt, H., Giustiniano, F. & Eda, G. Electronic transport properties of transition metal dichalcogenide field-effect devices: surface and interface effects. *Chem. Soc. Rev.* **44**, 7715–7736 (2015).
25. Chhowalla, M. et al. The chemistry of two-dimensional layered transition metal dichalcogenide nanosheets. *Nat. Chem.* **5**, 263–275 (2013).
26. Hadjichristidis, N., Pispas, S., & Floudas, G. Block copolymers: synthetic strategies, physical properties, and applications. (John Wiley & Sons, 2003).
27. Chou, S. Y., Krauss, P. R., Zhang, W., Guo, L. & Zhuang, L. Sub-10 nm imprint lithography and applications. *J. Vac. Sci. Tech. B* **15**, 2897–2904 (1997).
28. Ly, T. H. et al. Vertically conductive MoS<sub>2</sub> spiral pyramid. *Adv. Mater.* **28**, 7723–7728 (2016).
29. Splendiani, A. et al. Emerging photoluminescence in monolayer MoS<sub>2</sub>. *Nano Lett.* **10**, 1271–1275 (2010).
30. Mak, K. F., Lee, C., Hone, J., Shan, J. & Heinz, T. F. Atomically thin MoS<sub>2</sub>: a new direct-gap semiconductor. *Phys. Rev. Lett.* **105**, 136805 (2010).
31. Goldie, B. & Kapsanis, K. Corrosion under insulation: basics and resources for understanding. *J. Prot. Coat. Linings* **7**, 34–37 (2009).
32. Ruaan, R. C., Chou, H. L., Tsai, H. A., Wang, D. M. & Lai, J. Y. Factors affecting the nodule size of asymmetric PMMA membranes. *J. Membr. Sci.* **190**, 135–145 (2001).
33. Landau L. D., Lifshitz E. M. Elasticity theory. (Pergamon Press, 1975).
34. Leng, A., Streckel, H. & Stratmann, M. The delamination of polymeric coatings from steel. Part 1: calibration of the Kelvinprobe and basic delamination mechanism. *Corros. Sci.* **41**, 547–578 (1998).
35. Hu, R. G., Zhang, S., Bu, J. F., Lin, C. J. & Song, G. L. Recent progress in corrosion protection of magnesium alloys by organic coatings. *Prog. Org. Coat.* **73**, 129–141 (2012).



**Open Access** This article is licensed under a Creative Commons Attribution 4.0 International License, which permits use, sharing, adaptation, distribution and reproduction in any medium or format, as long as you give appropriate credit to the original author(s) and the source, provide a link to the Creative Commons license, and indicate if changes were made. The images or other third party material in this article are included in the article's Creative Commons license, unless indicated otherwise in a credit line to the material. If material is not included in the article's Creative Commons license and your intended use is not permitted by statutory regulation or exceeds the permitted use, you will need to obtain permission directly from the copyright holder. To view a copy of this license, visit <http://creativecommons.org/licenses/by/4.0/>.

© The Author(s) 2018